

This is an electronic reprint of the original article. This reprint may differ from the original in pagination and typographic detail.

Experimental Study of Blast Furnace Hearth Drainage Based on Image Analysis

Liu, Weiqiang; Shao, Lei; Saxén, Henrik

Published in:
Steel Research International

DOI:
[10.1002/srin.202100142](https://doi.org/10.1002/srin.202100142)

Published: 22/05/2021

Document License
Unknown

[Link to publication](#)

Please cite the original version:

Liu, W., Shao, L., & Saxén, H. (2021). Experimental Study of Blast Furnace Hearth Drainage Based on Image Analysis. *Steel Research International*, 92(10), Article 2100142. <https://doi.org/10.1002/srin.202100142>

General rights

Copyright and moral rights for the publications made accessible in the public portal are retained by the authors and/or other copyright owners and it is a condition of accessing publications that users recognise and abide by the legal requirements associated with these rights.

Take down policy

If you believe that this document breaches copyright please contact us providing details, and we will remove access to the work immediately and investigate your claim.

Experimental Study of Blast Furnace Hearth Drainage Based on Image Analysis

Weiqliang Liu¹, Lei Shao^{2*}, Henrik Saxén^{1*}

Process and Systems Engineering Laboratory, Faculty of Science and Engineering, Åbo
Akademi University, Åbo 20500, Finland

Department of Ferrous Metallurgy, School of Metallurgy, Northeastern University,
Shenyang 110819, China.

*) Corresponding author, Lei Shao: shaolei@smm.neu.edu.cn

*) Corresponding author, Henrik Saxén: Henrik.Saxen@abo.fi

Abstract: A smooth hearth drainage is one of the key requirements for maintaining an efficient blast furnace operation. For achieving this, it is necessary to understand the hearth drainage behavior and the effect of related process parameters. To investigate the drainage, a set of experiments was conducted in a two-dimensional Hele-Shaw model, where the influence of the initial accumulated amount of molten liquids (iron and slag), blast pressure and slag viscosity on the drainage behavior were studied using water and oil as liquids. To quantify the findings, an image analysis-based algorithm was applied to extract drainage information that was used to analyze the effect of the mentioned process factors on the evolution of the liquid levels and volumes, flow rates, share oil in the outflow, and angle of the interfaces at the outlet. The paper also discusses the implications of the results for the operation of the blast furnace hearth.

Keywords: blast furnace, hearth drainage, iron and slag flow, image analysis

1. Introduction

Even though it is already facing growing competition, the blast furnace (BF) is likely to maintain a dominant position among the ironmaking processing units, where iron ores are reduced and melted to liquid iron (“hot metal”). To improve the overall efficiency and decrease the environmental impact of the ironmaking process, the working volume of the BF has been increasing. Along with growing size, higher production rates and lower coke rates, the drainage of hot metal and slag face problems caused by longer flow paths of the liquids and worse permeability of the coke bed in the hearth, i.e., the dead man. This can have adverse effects on the operation, e.g., disturbing the burden descent, gas flow in and from the raceway, and liquid outflow. A smooth hearth drainage is also important to minimize splashing and oxidation of the hot metal, and to prevent wear of the hearth refractory wall, taphole as well as runners, which can prolong the campaign life of the BF. Thus, a well-controlled drainage is a prerequisite of a stable and efficient BF operation.

The liquids are drained through tapholes drilled in the hearth sidewall,^[1] and during the drainage the dominant outflow pattern is a simultaneous flow of iron and slag. It is possible that only iron or slag flows in the beginning of the tap if a single phase is in contact with the inner end of the taphole as the tapping starts. If iron is the first phase to drain, the iron-slag interface will descend (when the iron outflow rate exceeds the inflow rate) and a period with two-phase outflow follows. During this, pressure loss in the viscous slag phase leads to a lower pressure at the inner end of the taphole, which makes it possible to drain iron from lower levels. Therefore, the local iron-slag interface bends upwards to the taphole. With time, as the slag surface approaches the taphole, the slag-gas interface bends downward towards the taphole, until gas starts flowing out, and the tap is ended by plugging the taphole with mud. Thus, both the slag-gas interface (referred to as “l-g interface”) and iron-slag interface (“l-l interface”) show bending, but in different directions. If, conversely, slag is in front of the taphole when the

tap starts, a period of slag-only flow from the taphole is followed by a two-liquids flow period, which starts when the iron-slag interface comes close enough to the taphole to lift the iron by the pressure gradient caused by the slag flow. The draining then proceeds as outlined above until gas bursts out. The complex behavior of the interfaces is thus due to density and viscosity differences of the two liquids, where a local pressure gradient is formed near the taphole by the accelerating flow of the highly viscous slag through the packed bed of coke.^[2-5]

To understand the complex hearth drainage phenomena, several researchers have undertaken studies by applying simplified small-scale cold models and numerical models. The pioneering work by Tanzil et al. first revealed by experiments in pilot models (of both Hele Shaw and packed-bed type) that the denser liquid could be drained from level well below the taphole,^[2,3] which revised earlier findings of BF drainage.^[6] The observation was also explained based on basic concepts of fluid dynamics.^[2] Zulli extended the experimental and numerical work to consider a three-dimensional system and the effect of a dead man with a coke-free region, proposing expressions for a dimensionless flow-out coefficient.^[4] Nouchi^[7] carried out experiments in a small three-dimensional model using zinc chloride and silicon oil as substitutes for iron and slag, and sampled the liquid outflow during the draining experiments. A topic studied was how a coke-free zone under a partially floating deadman affected the interfaces and the outflow patterns. He et al. undertook a series of experiments in both a Hele-Shaw model and a packed bed model, studying the effects of packing pattern, drainage rate, and coke-free region on the gas breakthrough time.^[8,9] Liu et al. applied a Hele-Shaw model to study how, e.g., the initial amount of the liquids and the pressure difference, affected the tapping time, the liquid interfaces and the residual liquid ratios.^[10]

Many computational models have also been developed to gain an understanding of factors affecting hearth drainage. Some of the approaches are based on a simplified treatment of the fluid flow, while other use computational fluid dynamics to study the behavior. Based on the

results of small-scale experiments, Nouchi developed a simplified model of the liquid levels and outflows, by which the system could be studied computationally.^[7] Iida et al.^[11,12] used the empirical expressions developed by Nouchi and applied them in simulations, which used a multi-pool model with low-permeability zones in the deadman to explain the imbalance of iron and slag tapped from two alternating tapholes. Brännbacka et al.^[13] developed a strongly simplified model of hearth drainage and considered the role of a floating dead man on the evolution of the liquid levels. The authors showed that the duration of the period of iron-only flow, called the slag delay, was strongly affected by the motion of the deadman. It was later demonstrated^[14] that this simple model of hearth drainage could reveal whether the deadman was sitting or floating in operating blast furnaces. Saxén^[15] extended the model to hearth operation with alternating tapholes (but with an inter-cast period) using, as in the work of Iida et al.^[11,12], multiple pools, and a deadman that may float or not. This was demonstrated to yield rather complex motion patterns of the liquid levels. A simple liquid-level model by Shao and Saxén^[16] incorporated a model of the taphole, assuming a stratified flow of iron and slag. More recently, Roche et al.^[17] presented a drainage model of a multi-taphole furnace based on a simplified treatment of the fluid flow, and demonstrated that the model was able to explain outflow patterns observed in a large BF.

To get more detailed information about the hearth drainage, some simulations also have been done based on CFD or CFD-DEM methods. Nishioka et al.^[18,19] established a three-dimensional CFD model of hearth drainage validated on data from an operating BF. The authors studied the effect of various in-furnace conditions (e.g., coke diameter, coke free space, the void fraction of the deadman) on the evolution of interface levels, drainage rates, etc. Park et al.^[20] employed a three-dimensional CFD model to study the the interface deformation for the two-phase fluids (i.e., gas and molten iron) flow in a BF. Vångö et al.^[21] established a CFD-DEM model with a dynamic deadman to examine the influences of a low-permeability region and a coke-free zone

on the hearth drainage. Bambauer et al.^[22] developed an overall model of the gas, solid and liquid flow in a (down-scaled) BF, and demonstrated the interaction of the liquid levels on the deadman floating and coke flow patterns in the hearth.

In summary, considerable efforts have been made to study the iron and slag drainage behavior in the BF hearth based on numerical models with different degrees of simplification. Indeed, there are many advantages of the numerical approach, e.g., low labor and economic cost, good information for visualization. However, it is still essential to investigate the hearth drainage by experimental methods to guide, calibrate, and validate the numerical models and to shed light on special phenomena. Most hearth drainage experiments have applied traditional data extraction and processing techniques to collect the experimental information. However, there are some limitations on the levels of detail about the drainage that can be obtained in this way, and an accurate systematic analysis of, e.g., the interface levels may become a laborious task. To easily access such process information and to gain a deeper understanding of the hearth drainage, a digital image analysis technique was developed by the present authors.^[23] The system can follow the liquid-liquid and liquid-gas interfaces in a Hele-Shaw model by a high-speed camera, filtering out noise and disturbances to provide an accurate estimate of how the interfaces evolve during the drainage experiments. In this work, the technique is employed to interpret a series of experiments undertaken at different operational conditions. This made a systematic study and a quantitative analysis of the drainage process in the Hele-Shaw model possible. Section 2 of the paper describes the experimental set-up and the image analysis technique. Section 3 presents the experimental conditions, followed by Section 4, where the results are presented and analyzed. The fifth and final section concludes the paper with some discussion and proposals for future work. The data of the experiments are provided as supporting information.

2. Experimental Set-up and Technique

2.1. Apparatus Arrangement and Procedure

To study the draining of two liquids, an experimental system was designed. As illustrated in **Figure 1**, it consists of two subsystems, i.e., drainage experiment system and image acquisition system. As the main subsystem, the drainage system includes water and oil reservoirs, lifting table, peristaltic pump, oil distributor, Hele-Shaw model, liquid receiver, and vacuum pump. The Hele-Shaw model is the core part of the system and simulates multiphase flow in a packed bed by an analogous slot model with inner dimensions $585 \text{ mm} \times 2 \text{ mm} \times 580 \text{ mm}$ (width \times thickness \times height). It consists of two transparent perspex plates spaced at a small distance (here 2 mm) by perspex strips (of 2 mm thickness) at the walls and the bottom. Bolts keep the system tight and 2 mm washers (depicted as gray circles in the figure) guarantee constant spacing of the plates. An inherent advantage of the Hele-Shaw model is the quasi two-dimensional rectangular arrangement with two transparent walls, which makes it is feasible to observe and record the liquid levels in the model by camera with low optical distortion. This is a prerequisite for the image analysis technology developed to analyze the experimental results. Since the bolts and washers introduce some unavoidable disturbance to the flows and images, special attention had to be devoted to how to treat the interfaces in these regions, as explained later in the paper. The outlet of the model, drilled through the sidewall strip, is connected with a hose to a liquid receiver, which is held at vacuum pressure. Before the experiment, a valve on the hose is closed and a certain sub-atmospheric pressure is set in the receiver by running a vacuum pump to partly evacuate air from it. Water is introduced into the model through a slot in its left side connected to a water container. Oil is next introduced through an oil distributor (connected to a group of thin pipes) by running a variable-speed peristaltic pump. By this procedure, a uniform oil layer can be created on the water layer, as indicated in Figure 1. After these initialization processes, the filling devices are removed.

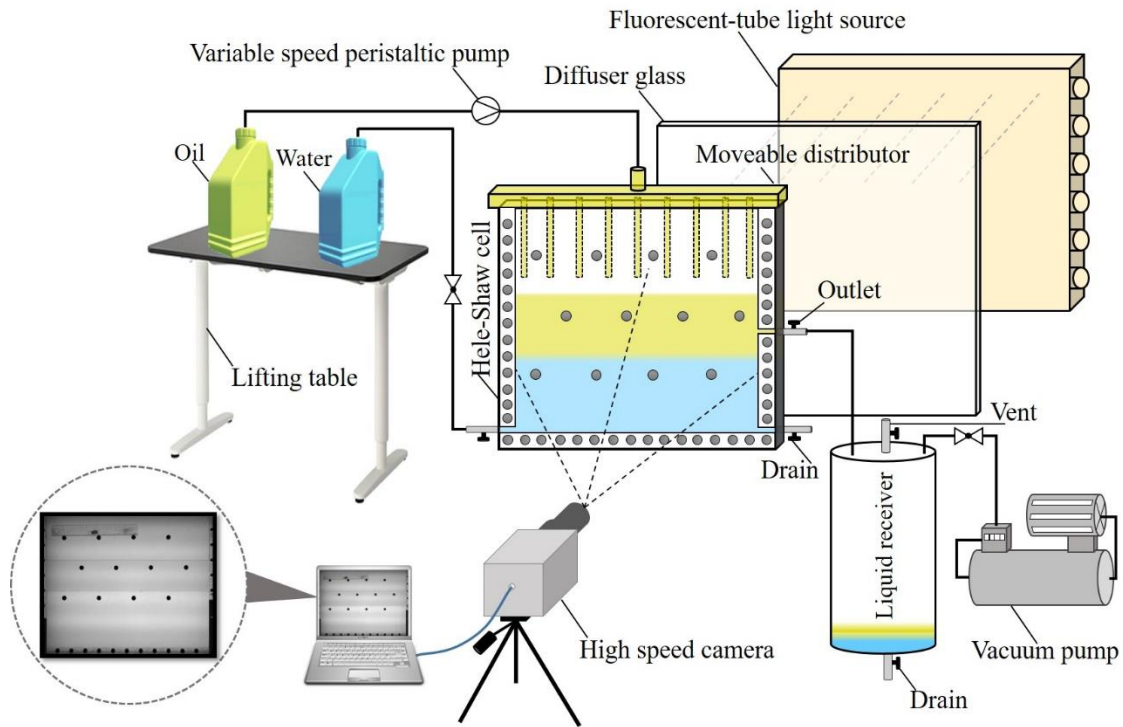


Figure 1. Schematic illustration of the set-up of the drainage experiments

The image acquisition system is designed for efficient data extraction and analysis. It includes a laptop with pertinent software, high-speed camera, diffuser glass, and light source. The high-speed camera is fixed in a position so the whole liquid zone of the Hele-Shaw model falls within the video frame. The laptop is connected to the camera for real-time display of the drainage process and for saving the recorded images. As a light source, a group of parallel fluorescence tubes are used on the opposite side of the Hele-Shaw model, with a diffuser glass placed between the model and the light source to create a uniform illumination. After starting the camera, the outlet valve is opened and the evolution of the descending interfaces is recorded until air escapes through the outlet and the experiment is stopped. More details about the Hele-Shaw model and ancillary equipment are reported elsewhere.^[10,23]

2.2. Image Analysis Algorithm

After the experiments, all the recorded images are treated by the digital image analysis algorithm, implemented in Matlab, to automatically extract desired information about the

drainage. The most critical step is an accurate interface extraction. Based on the extracted interfaces, some key drainage process parameters, e.g., liquid volumes and outflow rates, can be estimated. More detailed information can also be obtained, such as the slopes of the interfaces. A flowchart of the image analysis algorithm is presented in **Figure 2**: the algorithm includes sub-modules for image pre-processing, interface extraction and bending-point detection.

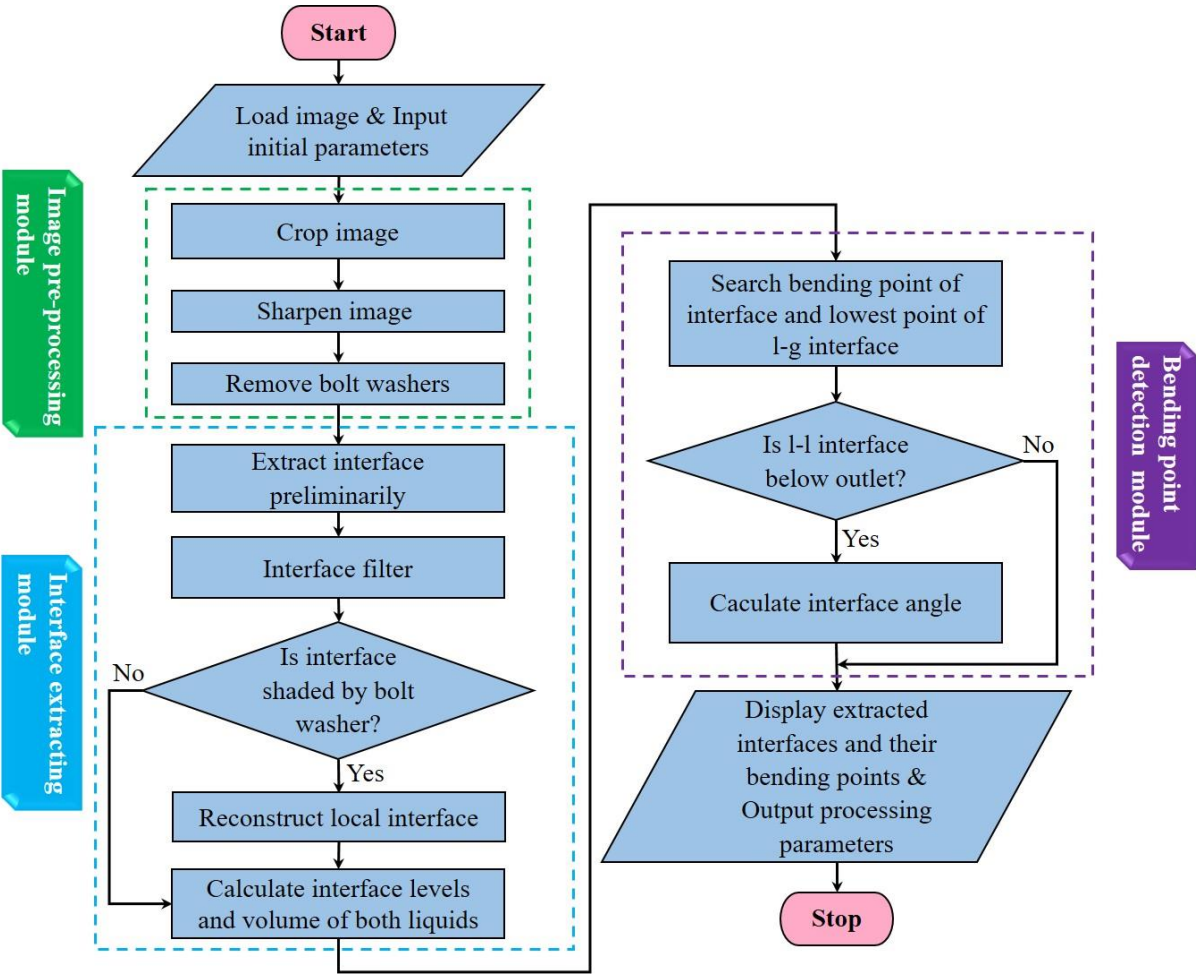


Figure 2. Flowchart of the digital image analysis algorithm.

The first module, image pre-processing, is a prerequisite for the later steps of the algorithm because it reduces the complexity of the subsequent image processing task, and thus improves the efficiency and accuracy of the algorithm. With reference to **Figure 3**, the pre-processing consists of three steps: cropping off the frame of the experimental drainage model ①,

sharpening the image ②, and removing the bolt washers ③ from the image. While the first pre-processing steps are rather straightforward, the third is more complicated and requires a detection of the bolts.^[23] Next, the pretreated images are used in the interface-extracting module, which accurately detects and extracts the interface profiles ④–⑥. The final module focuses on the local bending of the interfaces close to the outlet ⑦, e.g., for estimation of angles. At the termination of the procedure, the experimental image, extracted interfaces, and bending points are displayed together. Details of the image pre-processing module and interface extracting module are reported elsewhere.^[23] Compared to the original method, a new approach was here used for bending-point detection to improve the robustness, as described in subsection 4.3.

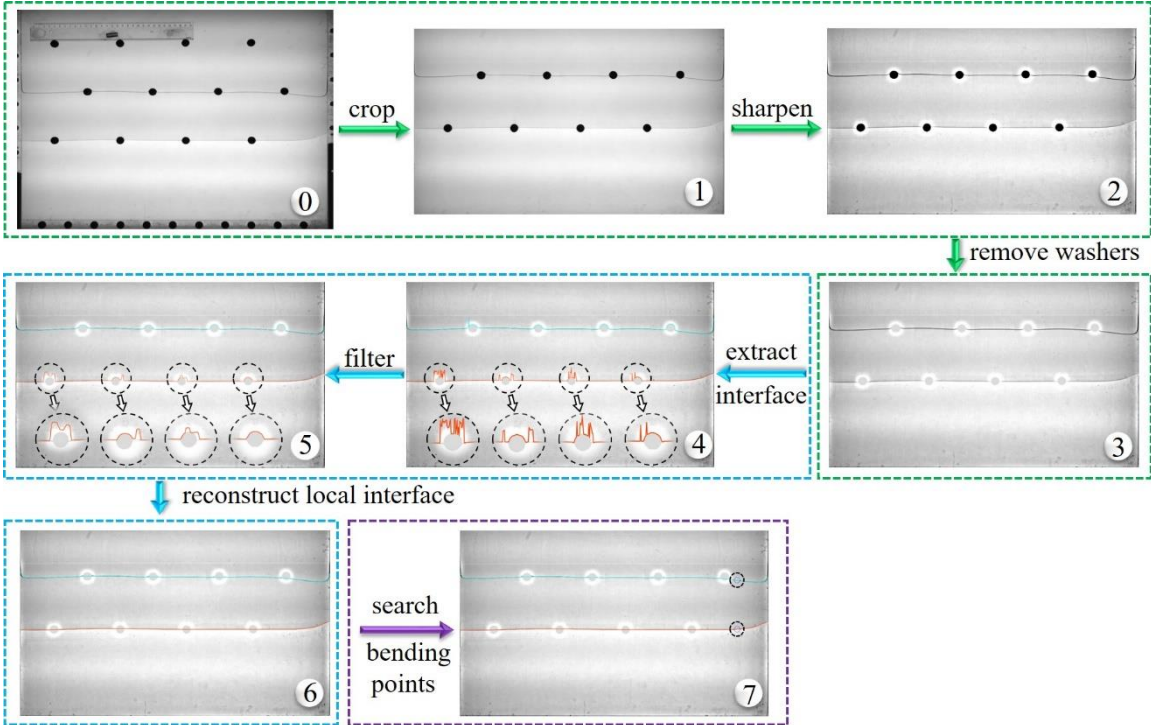


Figure 3. Graphical illustration of the main steps of the image analysis algorithm: cropping, sharpening, interface extraction, filtering and reconstruction, as well as bending point and angle detection.

3. Experimental Conditions

For a stable and efficient BF operation and an efficient drainage, it is essential to keep the accumulated liquid volumes (and the liquid levels) below certain limits in the hearth. Therefore, it is important to understand the effects of in-furnace conditions on the evolution of the levels of the interfaces and liquid volumes. The levels of the interfaces at the time when the taphole is opened depend on the drainage of the previous tap, the length of the time period between the taps, on the production rates of iron and slag, etc. Factor such as furnace pressure, deadman porosity and slag viscosity, which depends on temperature and composition, also play important roles. A varying slag-layer thickness at tap start can arise in multi-taphole blast furnace due to an imbalance in the slag flow from the alternating tapholes, as reported in the literature.^[11,12,17] To gain an understanding of some of these factors, a set of experiments were undertaken with the pilot model, as explained below.

Water and mineral oil in the Hele-Shaw model were used to emulate the molten iron and slag in the BF hearth, with physical properties listed in **Table 1**. The temperature of the liquids was kept fixed (at 21°C) in the experiments to guarantee that the viscosities stayed constant. The corresponding properties of iron and slag are also reported in the table.

Table 1. Physical properties of fluids in the blast furnace (BF) and model system

| Properties | System | |
|--|--------------------|-----------------------|
| | BF: 1:iron, 2:slag | Model: 1:water, 2:oil |
| Density of phase 1, $\rho_{1,1}$ (kg m ⁻³) | 6800 | 998 |
| Dynamic viscosity of phase 1, $\mu_{1,1}$ (Pa s) | 0.0068 | 0.001 |
| Density of phase 2, $\rho_{1,2}$ (kg m ⁻³) | 2800 | 855 |
| Dynamic viscosity of phase 2, $\mu_{1,2}$ (Pa s) | 0.43 | 0.131, 0.254 |

The experimental conditions of the batch drainage experiments (i.e., without liquid inflow) are reported in **Table 2**, where the first experiment acts as a reference for the forthcoming ones.

In the table, the pressure difference (Δp) is the difference between the atmospheric pressure (which acts on the top of the oil layer) and the pressure in the receiver. The initial liquid-liquid (l-l) interface level, $h_{l-l,0}$, is the level of the water-oil interface above the outlet. The initial oil-layer thickness, $h_{oil,0}$, is the absolute thickness of the oil layer, i.e., the difference of the initial levels of the two interfaces, $h_{oil,0} = h_{l-g,0} - h_{l-l,0}$, where $h_{l-g,0}$ is the initial liquid-gas (l-g) interface level. The oil viscosity was affected by changing the oil type.

Table 2. Experimental conditions with perturbed parameters written in bold.

| Experimental number | Δp bar | Oil viscosity Pa s | Initial l-l interface level mm | Initial oil-layer thickness Mm |
|---------------------|-------------------|-----------------------|-----------------------------------|-----------------------------------|
| 1 | 0.3 | 0.131 | 10 | 100 |
| 2 | 0.2 | 0.131 | 10 | 100 |
| 3 | 0.4 | 0.131 | 10 | 100 |
| 4 | 0.3 | 0.254 | 10 | 100 |
| 5 | 0.3 | 0.131 | 5 | 100 |
| 6 | 0.3 | 0.131 | 20 | 100 |
| 7 | 0.3 | 0.131 | 10 | 60 |
| 8 | 0.3 | 0.131 | 10 | 80 |

4. Results and Discussion

This section presents results of the experiments, provides explanations of the observed behavior and discusses the findings. The results of the experiments listed in Table 2 have been provided as supporting information in a spreadsheet file.

4.1 Liquid Levels and Volumes

The drainage under different conditions was studied by observing and depicting the time evolution of the overall liquid levels and volumes, calculated based on the location of the interfaces. To facilitate a comparison, the levels and volumes were also depicted with respect to normalized time, expressed as t/t_{total} , where t_{total} is the total draining time.

4.1.1. Effect of initial oil-layer thickness (Experiments 1, 7 and 8)

Experiments 1, 7 and 8 (cf. Table 2) were designed to study the effect of the initial thickness of the oil layer. The evolutions of the average liquid levels and liquid volumes are illustrated in **Figure 4**, in absolute (left panels) and normalized (right panels) time. The left top panel illustrates that the average l–g interface levels (upper red lines) evolve in parallel while the l–l interface levels evolve practically identically. The differences in the end points of the l–g level (top right panel) are smaller, because of a longer drainage time for the cases with thicker oil layer: the longer draining time lowers the average l–l interface level, so more oil and water can be drained. It is also observed that the lower l–l end level results in a higher l–g end level. The reason for this is that a lower water level will increase the proportion and flow rate of oil in the outflow, which yields a larger pressure loss in the bed^[2] (cf. subsection 4.2).

The lower panels of the figure show that the decrease of the oil volume is very small compared to the decrease of water and total volume with the tapping, which means that water is dominant fluid in the total outflow. For a thicker oil layer, the residual oil volume increases, but the water volume decreases.

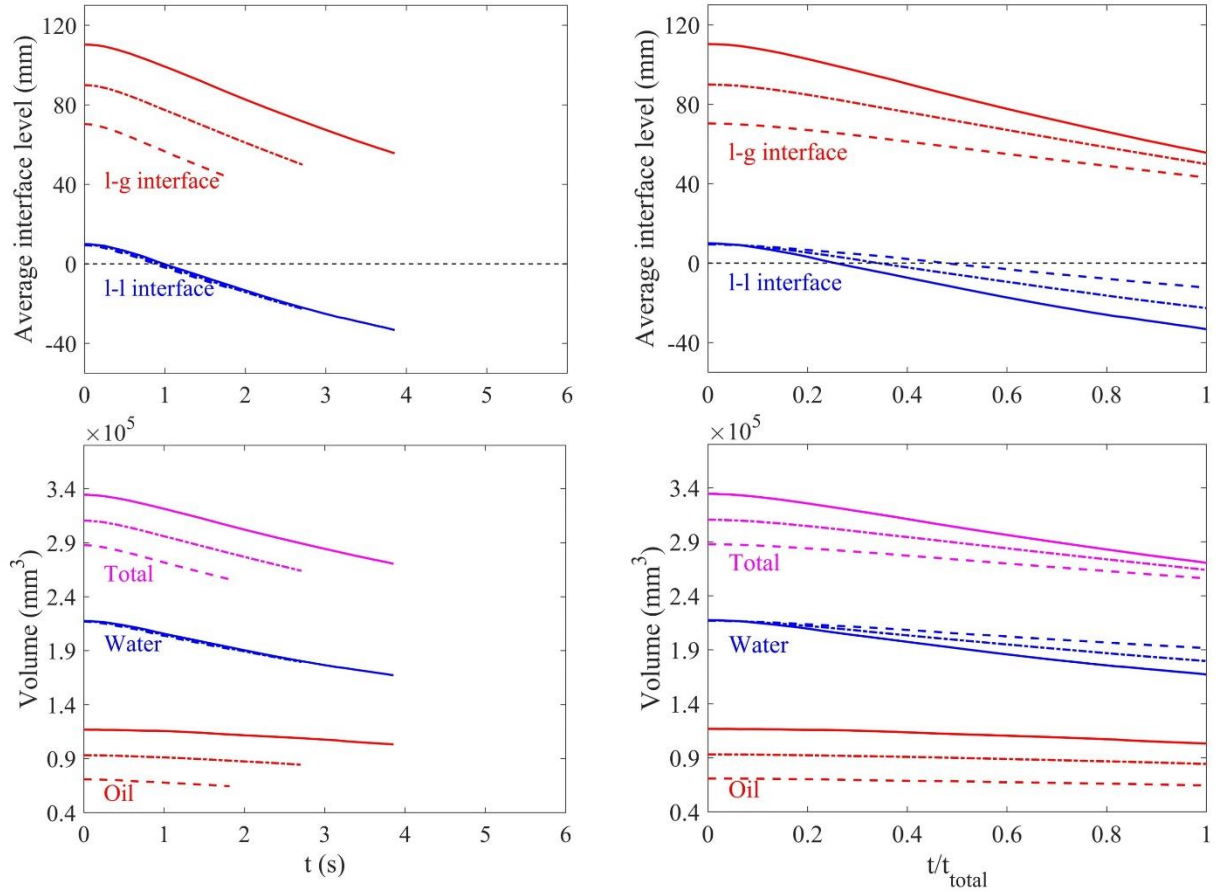


Figure 4. Effect of initial oil-layer thickness (60 mm: dashed line, 80 mm: dash-dotted line, 100 mm: solid line) in absolute (left panels) and normalized (right panels) time. Upper panels: Evolution of the average interface levels. Lower panels: Evolution of oil, water, and total volumes in the model. Pressure difference: 0.3 bar, oil viscosity: 0.131 Pa s, and initial l-l interface level: 10 mm.

4.1.2. Effect of pressure difference (Experiments 1-3)

The role of the pressure difference on the evolutions of average interface levels and liquid volumes is reported in **Figure 5**. The upper panel shows that the descent rate of the l-g and l-l interfaces increase with the pressure difference, but also that the faster drainage results in more residual oil and water at the tap end, as also seen in the lower panels. Thus, a small pressure difference results in a better draining. However, in the BF, a low blast pressure would extend the tap duration, which limits the production rate of the furnace and furthermore results in more extensive wear of the taphole. The blast pressure also affects the gas volumes in the furnace, which has implications for the pressure drop of the gas phase. Thus, a compromise solution must be considered in the real operation. Finally, it should be noted that the pressure drop in the experiments is largely caused by the drop in the channels from the outlet to the receiver, as

analyzed in detail in the Appendix, which explains the large pressure difference applied in the present system.

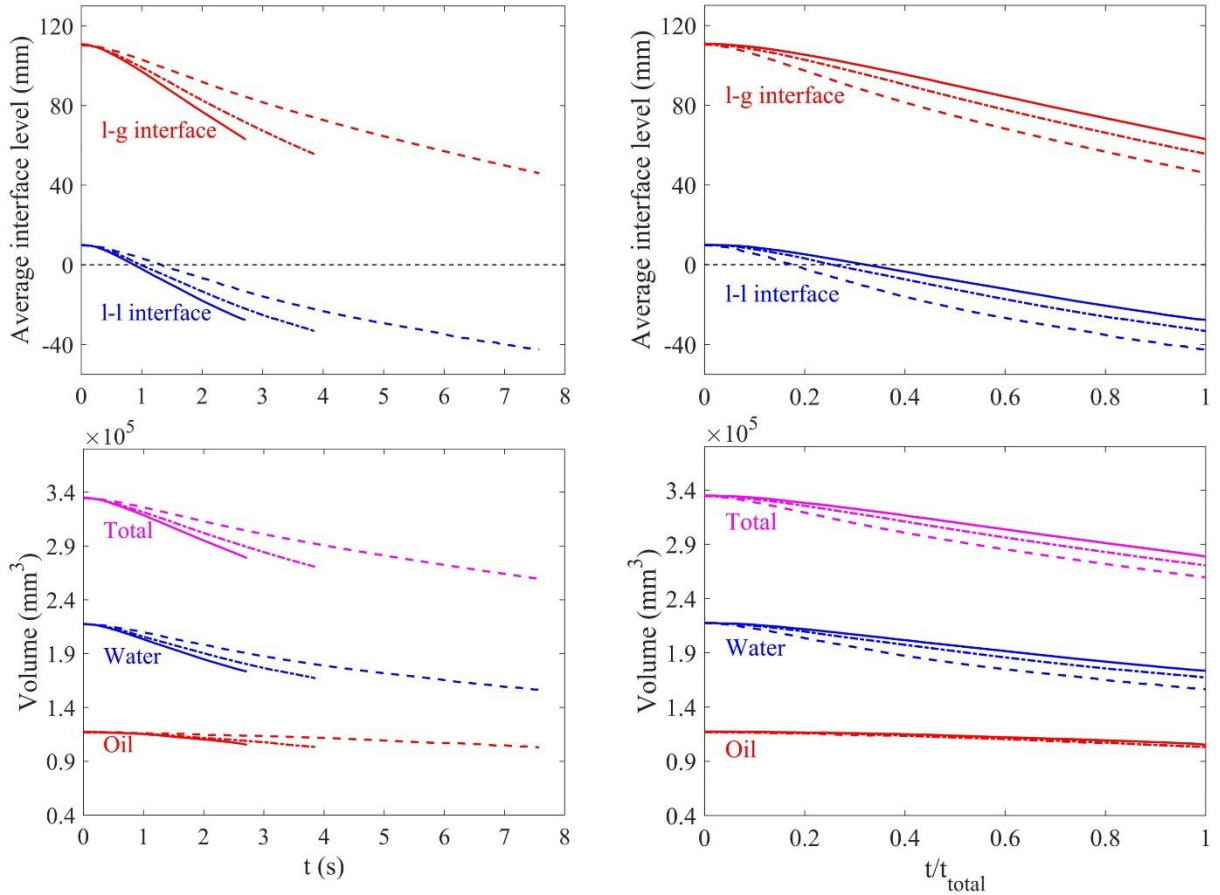


Figure 5. Effect of pressure difference (0.2 bar: dashed line, 0.3 bar: dash-dotted line, 0.4 bar: solid line) in absolute (left panels) and normalized (right panels) time. Upper panels: Evolution of the average interface levels. Lower panels: Evolution of oil, water, and total volume. Initial oil-layer thickness: 100 mm, oil viscosity: 0.131 Pa s and initial l-l interface level: 10 mm.

4.1.3. Effect of initial l-l interface level (Experiments 1, 5 and 6)

Figure 6 shows how the average interface levels and liquid volumes evolve for different initial l-l interface levels (5 mm, 10 mm and 20 mm). Naturally, the initial l-l level mainly affects the time it takes for the interface to descend close to the outlet (i.e., the moment when oil starts flowing out) and the total duration of the draining. These matters are further discussed in subsection 4.2. The initial l-l level is seen to have no effect on the end levels of the interfaces

(cf. top right panel): it only depends on the initial oil thickness, which is constant here (100 mm).

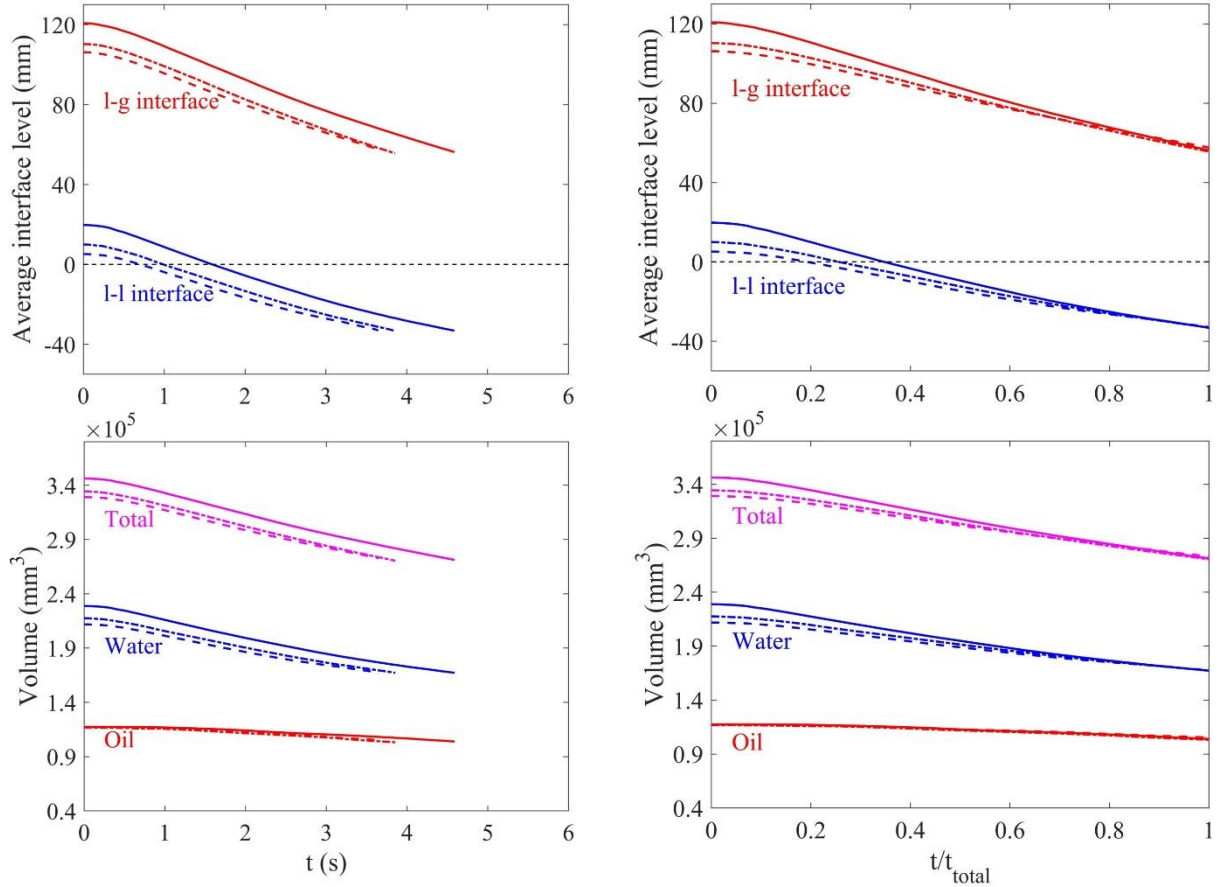


Figure 6. Effect of initial l-l level (5 mm: dashed line, 10 mm: dash-dotted line, 20 mm: solid line) in absolute (left panels) and normalized (right panels) time. Upper panels: Evolution of the average interface levels. Lower panels: Evolution of oil, water, and total volume. Initial oil-layer thickness: 100 mm, oil viscosity: 0.131 Pa s and pressure difference: 0.3 bar.

4.1.4 Effect of oil viscosity (Experiments 1 and 4)

Figure 7 shows how an increase in the oil viscosity affects the evolution of the average interface levels and liquid volumes. The outflow rate is seen to decrease with the oil viscosity, which prolongs the duration of the draining, but expressed in normalized time (right panels) the interface levels and liquid volumes are practically identical. This is due to the fact that the main pressure drop is caused by the flow of the more viscous phase (oil) and that it, for laminar flow, is proportional to the product of velocity and viscosity. Thus, changing one factor results in an inverse change in the other if the product remains constant.

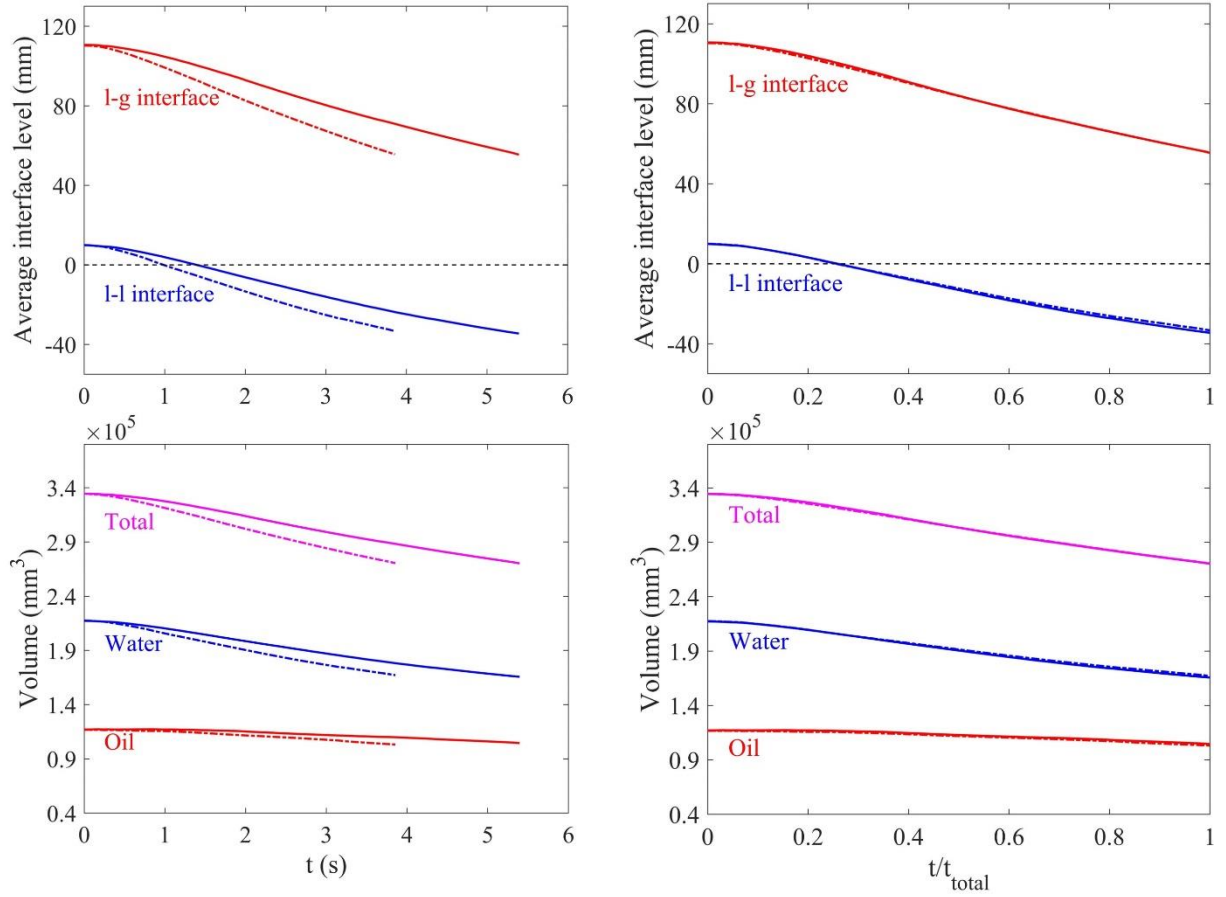


Figure 7. Effect of oil viscosity (0.131 Pa s: dash-dotted line, 0.254 Pa s: solid line) in absolute (left panels) and normalized (right panels) time. Upper panels: Evolution of the average interface levels. Lower panels: Evolution of oil, water, and total volume. Initial oil-layer thickness: 100 mm, initial l-l interface level: 10 mm, and pressure difference: 0.3 bar.

4.2. Outflow Rates and Oil Ratio

In order to gain a deeper understanding of the drainage behavior, the evolution of the liquid outflow rates and the slag ratio in the outflow were studied. Both can be determined by sampling the outflow, but this requires special and quite complex procedures (e.g., a carousel sampler such as the one applied by Nouchi et al.^[7]). However, as the interface levels are tracked relatively accurately in the present model, it is straightforward to integrate the liquid region based on the detected interfaces.^[23] In the forthcoming subsections, the outflow rates and the oil ratio (i.e., the volume flowrate of oil divided by the volume flowrate of water) are depicted in absolute and normalized time.

4.2.1 Effect of initial oil-layer thickness (Experiments 1, 7 and 8)

Figure 8 illustrates the influence of the initial oil-layer thickness on the evolution of the outflow rates and oil ratio. The upper panels show that a thicker initial oil layer leads to a more substantial drop in the outflow rate of water as the drainage approaches the end. Consequently, as seen in the lower panels, the oil ratio increases, particularly for the case with the largest initial oil-layer thickness. The reason for this is that an increased initial oil-layer thickness prolongs the tapping, which yields lower water levels at the end of the draining and therefore a larger draining resistance to flow of this liquid. The influence of the initial oil-layer thickness on the oil outflow rate is still very small, but sufficient to slightly elevate the end level of the l-g interface (cf. top panels of Figure 4).

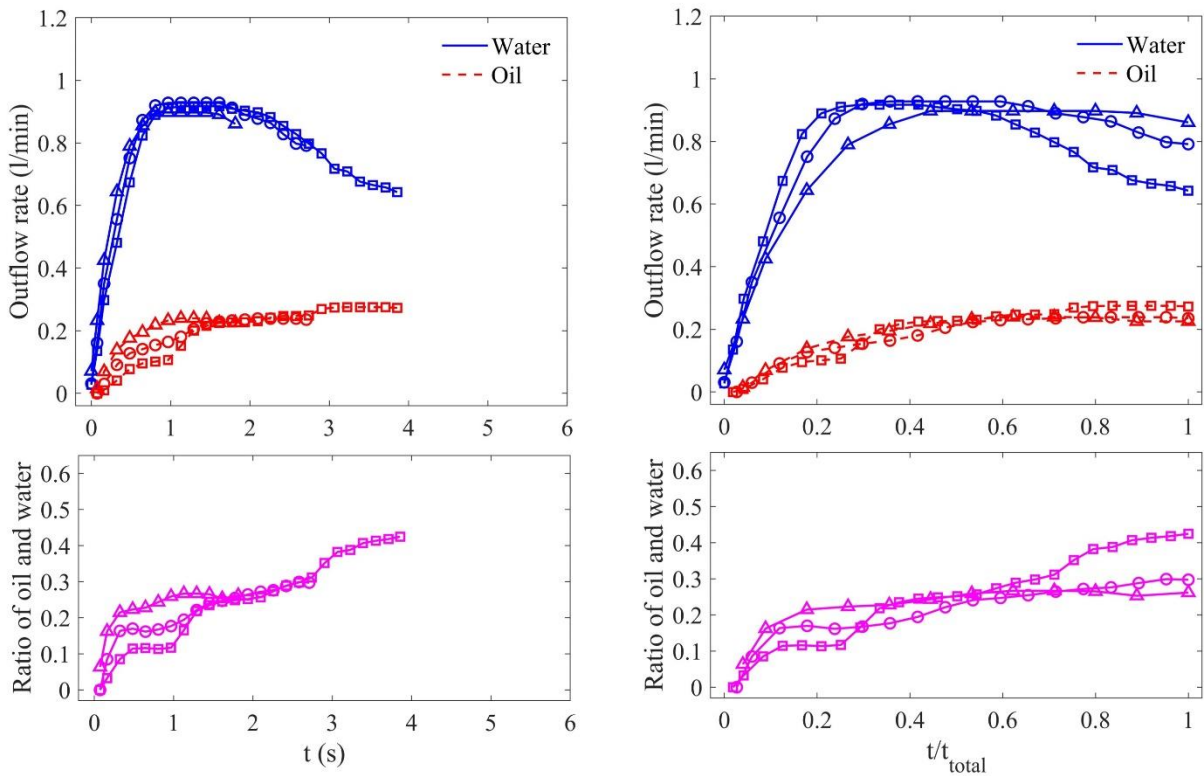


Figure 8. Effect of initial oil-layer thickness (60 mm: triangles, 80 mm: circles, 100 mm: squares) in absolute (left panels) and normalized (right panels) time. Upper panels: Evolution of the outflow rates. Lower panels: Evolution of ratio of oil and water. Initial l-l interface level: 10 mm, oil viscosity: 0.131 Pa s, and pressure difference: 0.3 bar.

4.2.2 Effect of pressure difference (Experiments 1-3)

The role of the pressure difference on the outflow rates is shown in the upper panels of **Figure 9**, which demonstrate that the flow of both oil and water increase dramatically with the pressure difference. The lower panels of the figure show that the effect of the pressure difference on the oil ratio in normalized time is quite small, and that the ratio slightly decreases with the pressure difference in the final parts of the drainage. This is associated with the lower l-l interface which promotes oil flow (cf. lower panels of Figure 5).

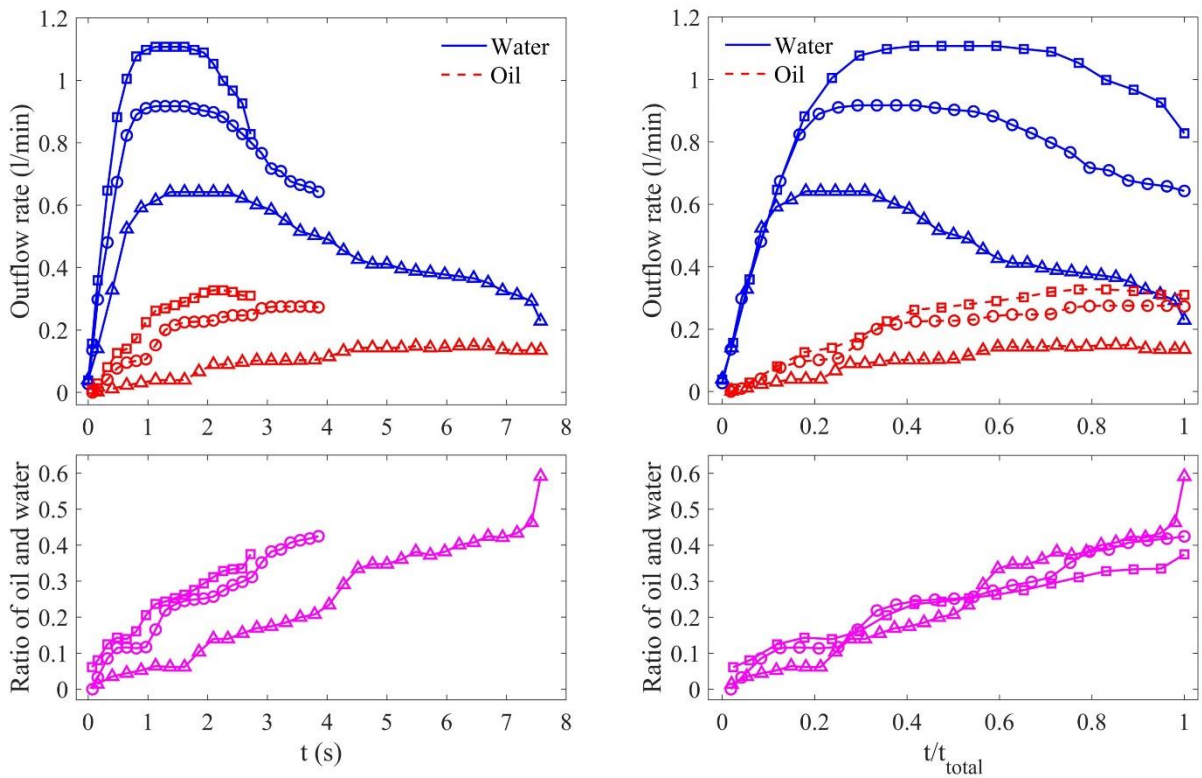


Figure 9. Effect of pressure difference (0.2 bar: triangles, 0.3 bar: circles, 0.4 bar: squares) in absolute (left panels) and normalized (right panels) time. Upper panels: Evolution of the outflow rates. Lower panels: Evolution of ratio of oil and water. Initial oil-layer thickness: 100 mm, initial l-l interface level: 10 mm, and oil viscosity: 0.131 Pa s.

4.2.3 Effect of initial l-l interface level (Experiments 1, 5 and 6)

Figure 10 illustrates that the effect of the initial l-l interface level on the evolution of the outflow rates and oil ratio is less significant but logical: a higher level promotes initial water outflow and the highest level studied (20 mm) yields a period of water-only flow during the

first fractions of a second. For the later parts of the draining and in normalized time, the oil ratio is practically the same in the three cases (cf. bottom right panel).

In the practical operation, the initial l-l level can be sensed by observing the outflow orders of iron and slag from the furnace at the tappings, and the slag delay (i.e., the time of iron only flow in the beginning of the tap) has been demonstrated to be an important indicator of the hearth state.^[13,14,17,24]

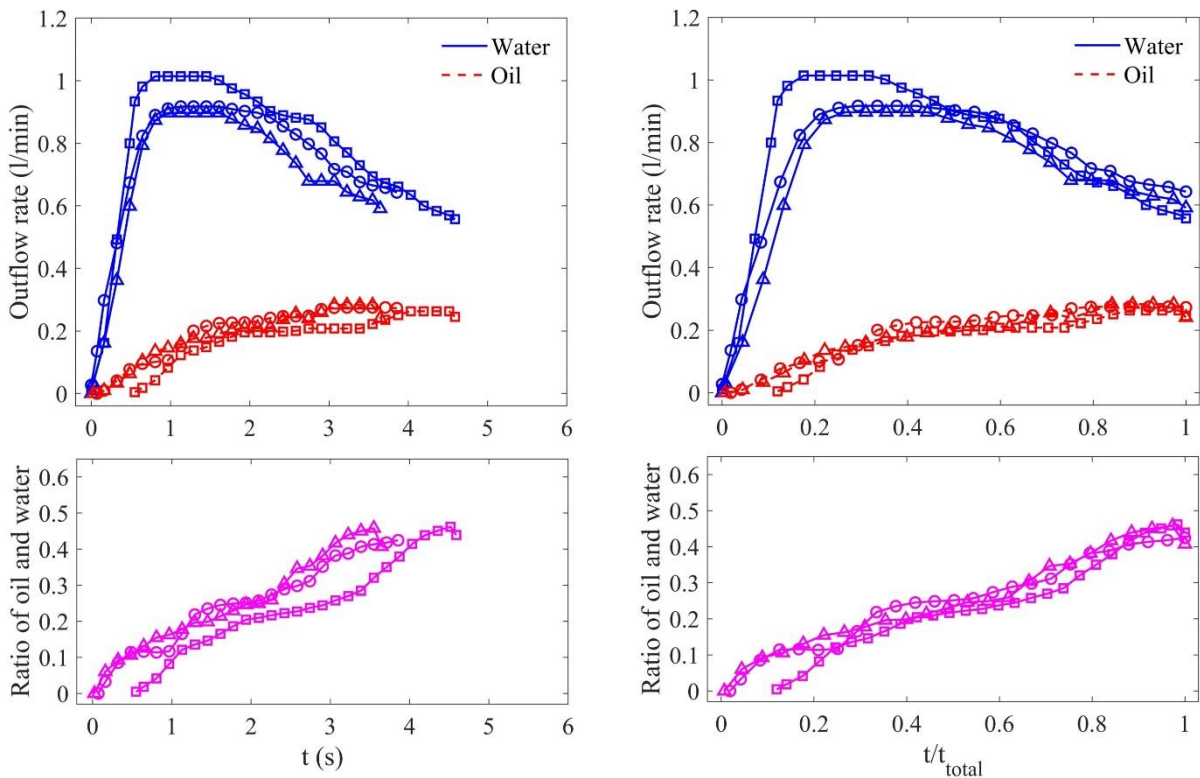


Figure 10. The effect of initial l-l interface level (5 mm: triangles, 10 mm: circles, 20 mm: squares) in absolute (left panels) and normalized (right panels) time. Upper panels: Evolution of the outflow rates. Lower panels: Evolution of ratio of oil and water. Initial oil-layer thickness: 100 mm, oil viscosity: 0.131 Pa s, and pressure difference: 0.3 bar.

4.2.4 Effect of oil viscosity (Experiments 1 and 4)

Finally, the effect of oil viscosity on the outflow rates is presented in the upper panels of **Figure 11**, illustrating that the outflows of both oil and water decrease with the oil viscosity. This is caused by the increased flow resistance in the system when using a more viscous oil. As outlined in the Appendix, a major part of the pressure drop arises in the channels from the outlet

to the liquid receiver. The right bottom panel indicates that the evolution of the oil ratio in normalized time is very similar for the two cases, and the differences observed may be due to stochastic effects.

In practice, a high slag viscosity would call for a revised tapping strategy since a prolonged duration of the taps cannot (always) be accepted. A possible remedy is to use a larger diameter of the taphole drill bit, which increases the outflow rates, but this will have implications for the final slag level at the end of the tap, as discussed in subsection 4.1.2.

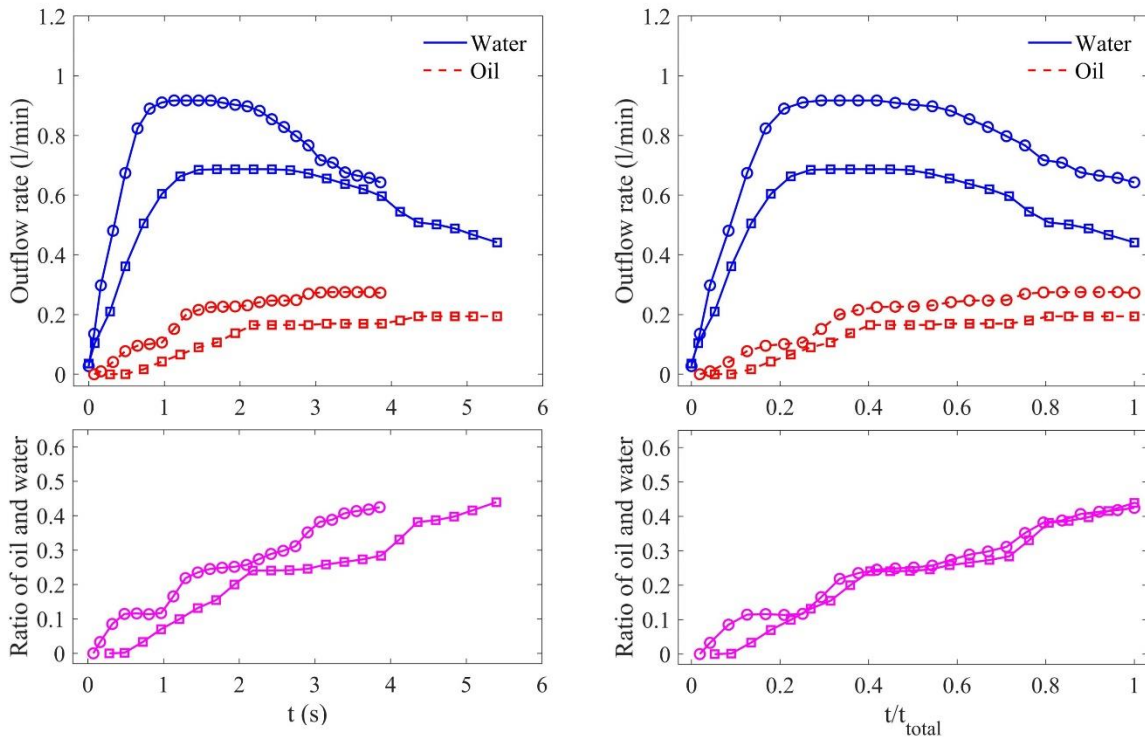


Figure 11. Effect of oil viscosity (0.131 Pa s: circles, 0.254 Pa s: squares) in absolute (left panels) and normalized (right panels) time. Upper panels: Evolution of the outflow rates. Lower panels: Evolution of ratio of oil and water. Initial oil-layer thickness: 100 mm, initial l-l interface level: 10 mm, and pressure difference: 0.3 bar.

4.3 Interface Angles

During BF hearth drainage, the interface profiles and the interface bending change continuously, and are affected by certain in-furnace conditions (like slag viscosity and deadman voidage). As discussed above, the tapping time is strongly related to the local bending of the l–

g interface. Thus, it is motivated to quantify the interface bending degree in the drainage experiments.

To illustrate the evolution of the interface bending visually, the local area close to the outlet was extracted from the experimental images. This area for one recorded experimental image is shown in **Figure 12**.

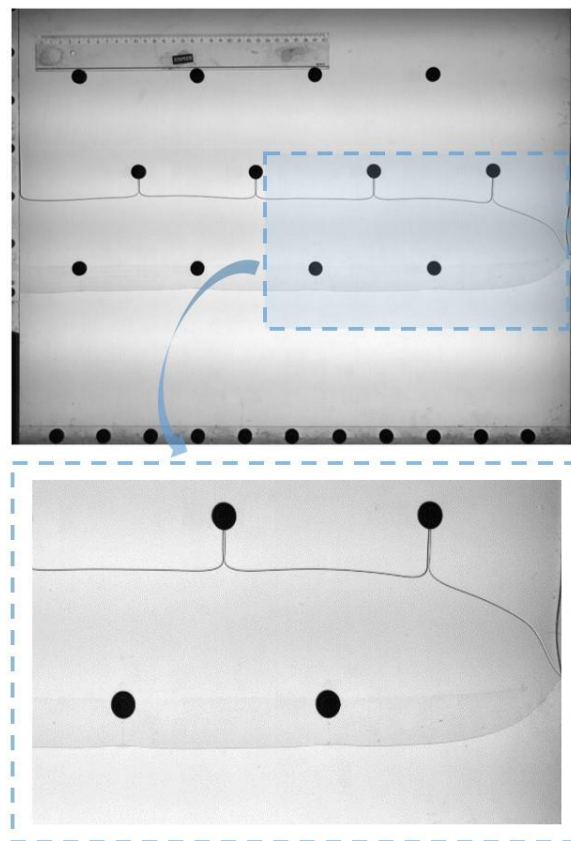


Figure 12. Locally extracted area in an image for the determination of the bending angle.

To quantitatively analyse the interface bending, two parameters, i.e., the l–g interface angle (α_{up}) and l–l interface angle (α_{down}) are introduced. The l–g interface angle is determined by the locations of lowest point and the bending point on the l–g interface, while for the l–l interface angle, the bending point and highest point on the l–l interface are used. The bending points are here defined as the intersection points of the interfaces and a vertical reference line placed at a

distance of one tenth of the width of the Hele-Shaw model from the outlet (cf. **Figure 13**). Thus, during the drainage process, the horizontal positions of the bending points remain fixed.

The l-g interface angle (α_{up}) and l-l interface angle (α_{down}) are calculated by

$$\alpha_{up} = \arcsin\left(\frac{\Delta h_{up}}{d_{up}}\right) \quad (1)$$

$$\alpha_{down} = \arcsin\left(\frac{\Delta h_{down}}{d_{down}}\right) \quad (2)$$

where d_{up} and Δh_{up} are the total and vertical distances between the bending point on the l-g interface and the lowest point of the interface, respectively, while d_{down} and Δh_{down} are the corresponding distances between the bending point on the l-l interface and the highest point of the interface. A schematic of the interface angles and the quantities used to determine them is provided in Figure 13.

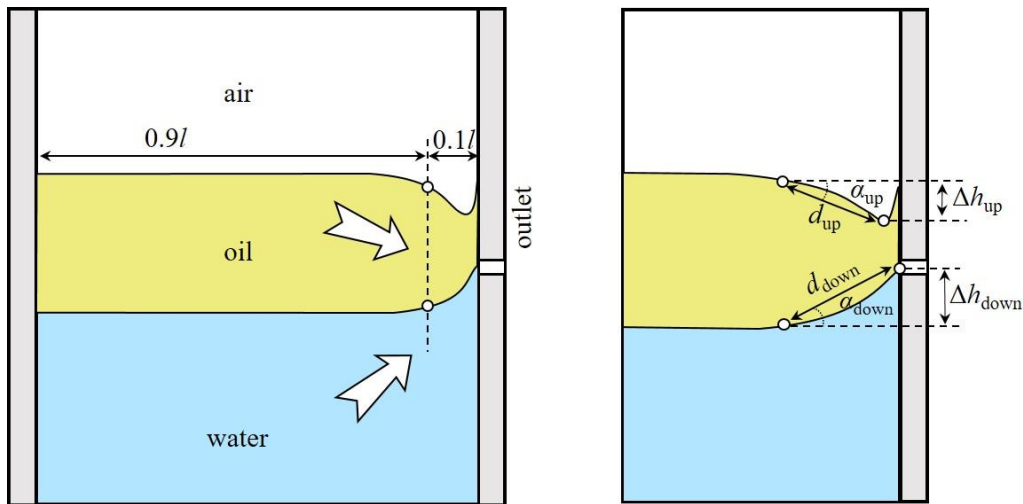


Figure 13. Schematic of interface angles and quantities used to determine them

4.3.1 Effect of initial oil-layer thickness (Experiments 1, 7 and 8)

The effect of the initial oil-layer thickness is first studied. The interfaces depicted in **Figure 14** (top row: 60 mm, middle row: 80 mm, bottom row: 100 mm) for three different times distributed uniformly over the drainage duration ($t/t_{total} = 1/3, 2/3$ and 1), and the bending angles shown in **Figure 15a** indicate that the l-l interface bending increases with the oil-layer thickness,

because a thicker oil layer means that the water level has more time to descend below the outlet. For the l-g interface, the changes of the bending angle are not significant until the end of the drainage, when it increases slightly. The latter can be explained by the (slightly) increased oil flow as the l-l level descends deeply below the outlet (cf. Figures 4 and 8). The time points depicted in Figure 14 are indicated by dashed vertical lines in Figure 15a, and the insert in the latter figure depicts the l-g interface angle in more detail at the final parts of the draining. Note the different scales for the l-l (left) and l-g (right) angles.

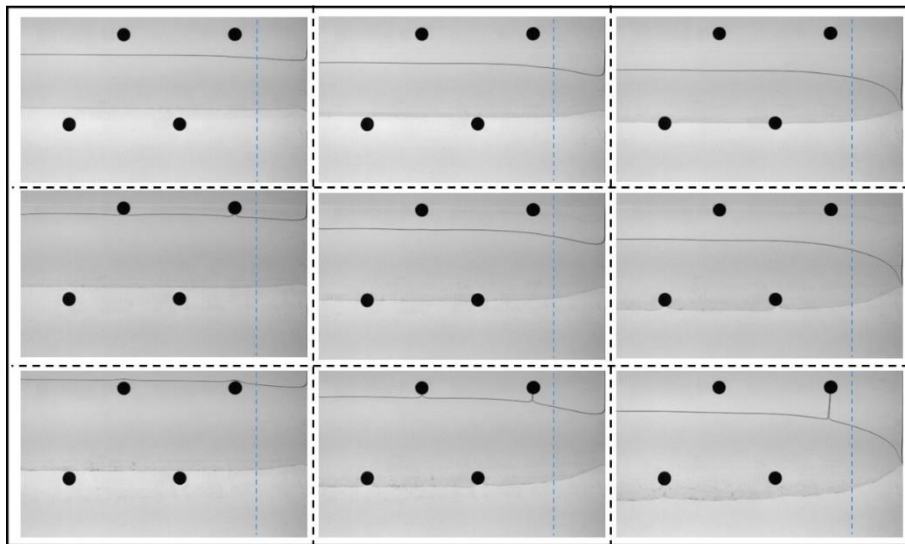


Figure 14. Effect of initial oil-layer thickness (top row: 60 mm, middle row: 80 mm, bottom row: 100 mm) on the evolution of interface bending. State after one third (leftmost panels), two thirds (center panels) and end (rightmost panels) of the drainage process. Experimental conditions: initial l-l interface level: 10 mm, pressure difference: 0.3 bar, and oil viscosity: 0.131 Pa s.

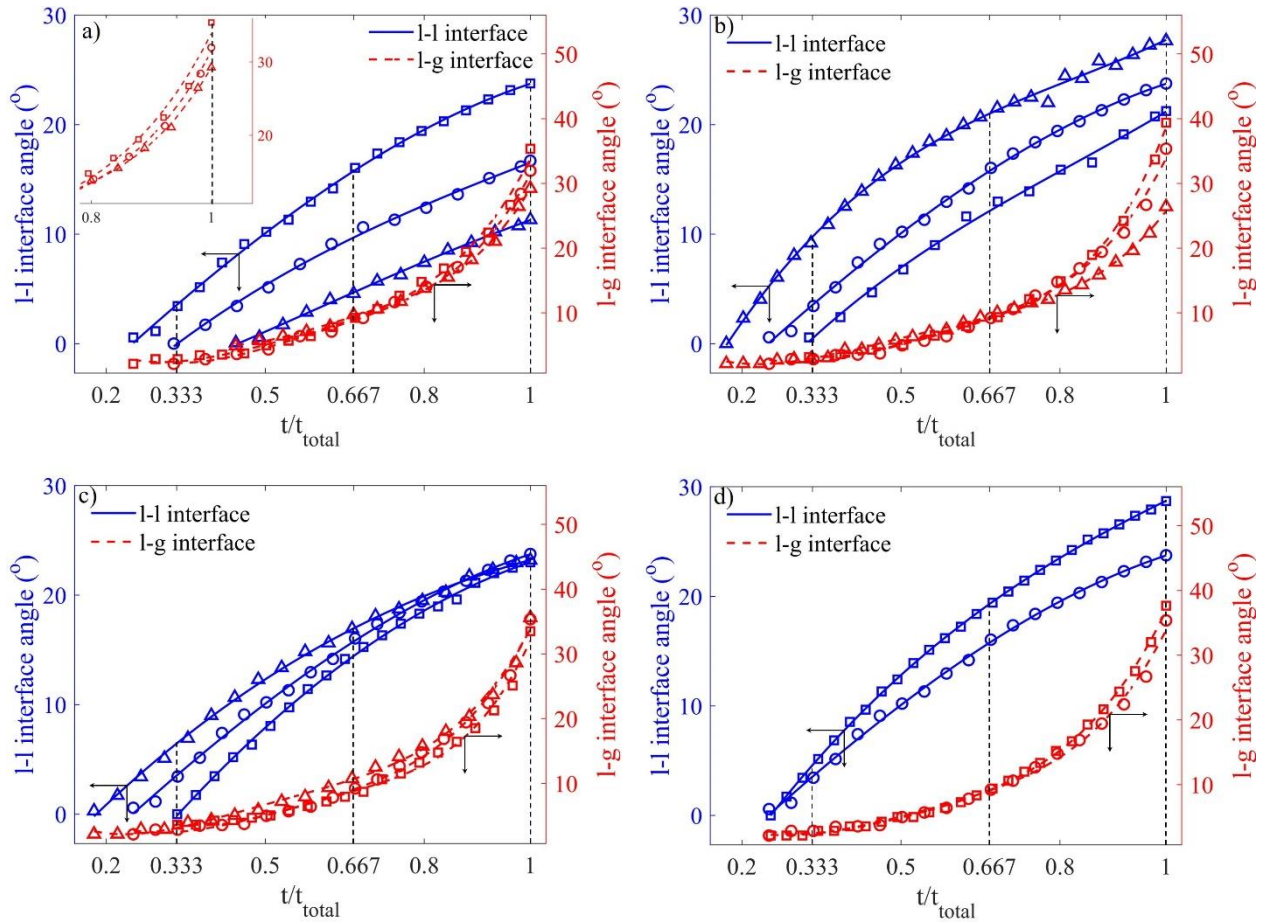


Figure 15. Effect of a) initial oil-layer thickness, b) pressure difference, c) initial l-l interface level, and d) oil viscosity on the bending of the l-l and l-g interfaces during the drainage. The studied variable increases when going from triangles, through circles to squares. The conditions are reported in Table 2.

4.3.2 Effect of pressure difference (Experiments 1-3)

A positive correlation of the pressure difference and the l-g interface angle near the end of the drainage process is seen in **Figure 15b**, which also shows that the l-l interface bending is affected in the opposite direction. The former is caused by a higher pressure gradient in the oil phase, while the latter reflects the shorter drainage time, which leaves more residual water at the end of the drainage. The end angle of the l-g interface for $\Delta p = 0.4$ bar is very close to 40° , which is the largest angle encountered among all experiments in this study.

4.3.3 Effect of initial l-l interface level (Experiments 1, 5, and 6)

Figure 15c shows the role of the initial l-l interface level on the interface bending. Both interfaces bend earlier and more for a lower initial l-l interface level, but the effect on the bending is stronger for the l-l interface. Again, these findings reflect how the initial l-l level

affects the time when oils starts flowing out and when the drainage ends. It may be observed that for different initial l-l interface levels, the difference in the l-l interface angle at the same normalized draining time decreases with the progress of the drainage, which also reflects the role of the tapping time.

4.3.4 Effect of oil viscosity (Experiments 1 and 4)

The oil viscosity influences the interface angles as illustrated in **Figures 15d** and **16**. Since the higher viscosity (squares in Figure 15d) leads to slower and therefore longer drainage, the l-l interface has more time to descend. The slight increase of the l-g interface angle is attributed to the higher pressure gradient in the oil, but the slower outflow (Figure 11) partly cancels this effect.

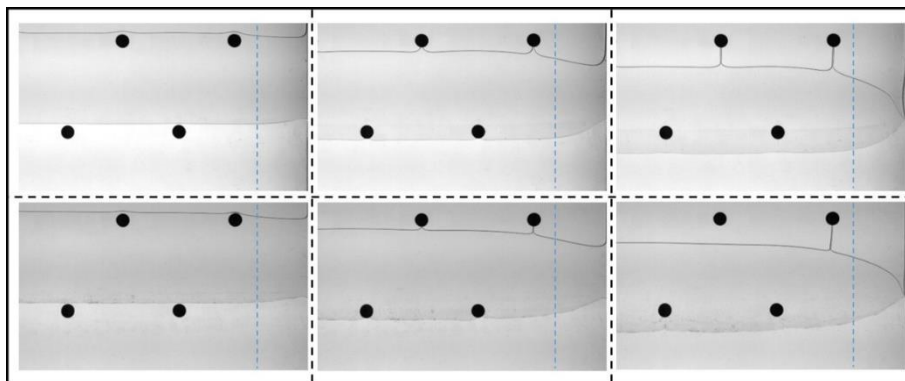


Figure 16. Effect of oil viscosity (top row: 0.254 Pa s, bottom row: 0.131 Pa s) on the evolution of interface bending. State after one third (leftmost panels), two thirds (center panels) and end (rightmost panels) of the drainage process. Experimental conditions: initial oil-layer thickness: 100 mm, pressure difference: 0.3 bar, and initial l-l level: 10 mm.

5. Conclusions and Practical Implications of the Findings

With the intent to gain a deeper understanding of the hearth drainage and factors that affect it in the blast furnace tapping process, a set of experiments have been undertaken in a two-dimensional Hele-Shaw model with oil and water as substituting liquids. The experiments were observed by video recording through the transparent perspex wall of the model and an image

analysis-based algorithm was applied to extract information from the trials. Compared to the traditional method, where images are manually analyzed, the present algorithm can extract more detailed information and makes it feasible to quantify the findings of drainage experiments. The main efforts in the work were focused on investigating the influence of the process parameters on the evolution of liquid-liquid (l-l) and liquid-gas (l-g) interface levels, liquid volumes, outflow rates, oil ratio in the outflow, as well as interface angles.

Based on the experimental results, the following conclusions can be made:

- 1) An increase of the initial oil-layer thickness decreases the residual water volume, but increases the residual oil volume. It also reduces the water outflow rate and raises the oil ratio at the end of the drainage.
- 2) With a more viscous oil, the oil and water outflow rates decrease considerably. Both interface angles increase, especially at the later stages of the drainage, due to the prolonged draining time.
- 3) Applying a higher pressure difference on the drainage system, the final interface levels, residual liquids volumes, outflow rates, and l-g interface angle increase. The l-l interface angle decreases and the oil ratio also decreases in the later stages of the drainage. It should here be noted that a major part of the the pressure difference imposed is needed to compensate for the substantial pressure drop outside the Hele-Shaw model in the pipeline to the receiver (cf. Appendix).
- 4) An increase of initial l-l interface level mainly prolongs the drainage, but yields almost identical levels of the interfaces at the end of the drainage.

The above findings are in general agreement with experimental and numerical findings by earlier investigators and also with practical observations in the casthouse of blast furnaces. For instance, outflow patterns with a growing slag ratio observed in many plants are supported by the experimental findings. Likewise, the large amount of residual iron and slag after “too fast”

taps can be explained. Also, the implication for subsequent taps of residual slag left in the hearth due to poor slag drainage of a single tap can be understood.

Future work will focus on how the experimental results could be used to express the internal pressure loss, considering the bending domains of the two phases, possibly also measuring local static pressure in the Hele-Shaw model. A CFD model of the Hele-Shaw model has also been developed, and the simplified expression of the pressure loss in the external pipes outlined in the Appendix will be incorporated to simulate the experimental system.

Supporting information: The main data of the experiments have been enclosed as supporting information in the file Liu_et_al_2021_Supplemental_data.xlsx.

Acknowledgments: This work was carried out with support from the Åbo Akademi Foundation, and this funding is gratefully acknowledged. The second author (LS) wishes to thank the National Natural Science Foundation of China (Grant 51604068) for providing financial support for this work.

Conflicts of Interest: The authors declare no conflict of interest.

Appendix

This appendix makes an attempt to theoretically estimate the pressure drop in the outlet piping of the Hele-Shaw model. **Figure A1** depicts the outlet piping schematically, showing four pipes and sudden expansions and reduction of diameters. The first section is the channel formed by a slot in the sidewall with a rectangular 2 mm × 2 mm cross section, while the rest have circular cross sections. Note that the scales in the schematic are not realistic.

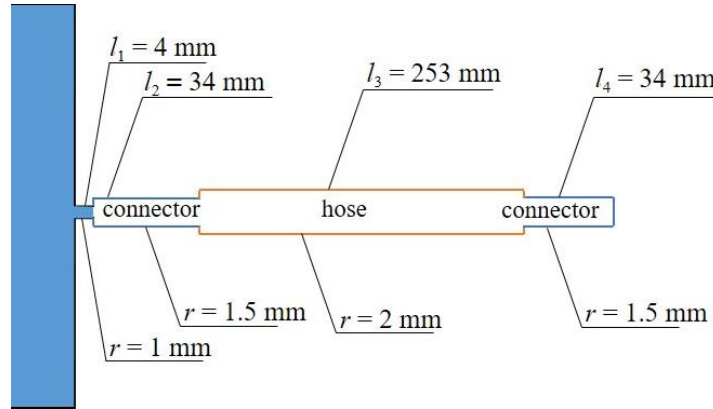


Figure A1. Schematic of the outlet pipes of the Hele-Shaw model.

Due to the slow flow rates and small diameters, the flow in the pipes is laminar throughout all experiments. A preliminary analysis of the system revealed that a simplified model of the pressure drop, using a volumetric weighing of the viscosity of oil and water, was not able to reproduce the measured pressure drops, but strongly overestimated them. The two-phase flow regime of oil and water in pipes is known to show various characteristics based on volume proportions, flow rates and viscosities (Brauner^[25]). Therefore, a simplified core-annular model proposed by Bensakhria et al.^[26] was applied, where the oil core flow may be asymmetrically located, thus possibly touching the pipe wall to some extent. The expression of the pressure loss per unit length for pipe section i is

$$\frac{\Delta p_i}{l_i} = (1 - \xi) \frac{8\mu_w \dot{V}_{\text{tot}}}{\pi(r_i^4 - r_{s,i}^4)} + \xi \frac{8\mu_o \dot{V}_{\text{tot}}}{\pi r_i^4} \quad (\text{A1})$$

where the core radius is given by

$$r_{s,i} = \frac{r_i}{\sqrt{1 + 2\dot{V}_w/\dot{V}_o}} \quad (\text{A2})$$

and where ξ is the relative contact perimeter, defined as the part of the core perimeter in contact with the wall divided by the wall perimeter.^[26] In addition to the pressure loss in the pipe sections, the losses in the elements, including inlet, expansions and reductions and outlet have to be considered. For these, expressions of the type

$$\Delta p = f_j \frac{\rho_{\text{tot}} w_i^2}{2} \quad (\text{A3})$$

were used, where f_j is the loss coefficient, ρ_{tot} is the mean density defined as $\rho_{\text{tot}} = (\dot{V}_w \rho_w + \dot{V}_o \rho_o) / \dot{V}_{\text{tot}}$ with $\dot{V}_{\text{tot}} = \dot{V}_w + \dot{V}_o$ and the velocity is given by $w_i = \frac{\dot{V}_{\text{tot}}}{A_i} = \frac{\dot{V}_{\text{tot}}}{\pi r_i^2}$. The inlet and outlet loss factors are $f_{\text{in}} = 0.5$ and $f_{\text{out}} = 2.0$, while for expansions and reductions we have^[27]

$$f_{\text{exp},i} = 2 \left[1 - \left(\frac{r_i}{r_{i+1}} \right)^4 \right] \quad (\text{A4})$$

$$f_{\text{red},i} = \left(1.2 + \frac{160}{\text{Re}_i} \right) \left[\left(\frac{r_i}{r_{i+1}} \right)^4 - 1 \right] \quad (\text{A5})$$

where r_i and r_{i+1} refer to the pipe radius before and after the element, respectively.

The pressure drop between the plates in the Hele-Shaw model was neglected here as it is only in the order of 0.01 bar, which is estimated by the Kozeny-Carman equation in the case of only oil flowing through the model.

These equations were applied to the four sections ($i = 1, \dots, 4$, see Figure A1) and the elements using the water and oil outflow rates measured in Experiments 1-3 (cf. Table 2 and Figures 5 and 9), where the pressure difference was varied. Since the factor ξ in Equation (A1) is unknown, and was noted to depend of the flow rate in the present work and in the investigations by Bensakhria et al.,^[26] with higher values (i.e., more contact of the oil core with the wall) at lower flow rates, it was hypothesized that the factor be inversely proportional to the flowrate. Using the expression

$$\xi = \frac{0.07 \frac{1}{\text{min}}}{\dot{V}_{\text{tot}}} \quad (\text{A6})$$

the calculated pressure drops over the pipe system illustrated in Figure A2 were obtained. Even though the initial pressure drop shows considerable differences to the measured value (most

likely due to the acceleration of the fluid in the hose as it is being filled), the figure indicates that the results can be explained at least qualitatively. The fact that the simulated pressure drop decreases during the last part of the draining, i.e., the true system experiences a larger loss than predicted by the mathematical model, suggests this may be associated with a different mixing of the two phases. Scrutiny of the top right panel of Figure 5 reveals that the time points when the l-l interface has descended 15 mm below the outlet roughly correspond to the points in Figure A2 where the downward slope of the calculated pressure drop occurs. This supports the theory that such mixing occurs as the water enters the outlet from below, distorting the flow field in the pipes.

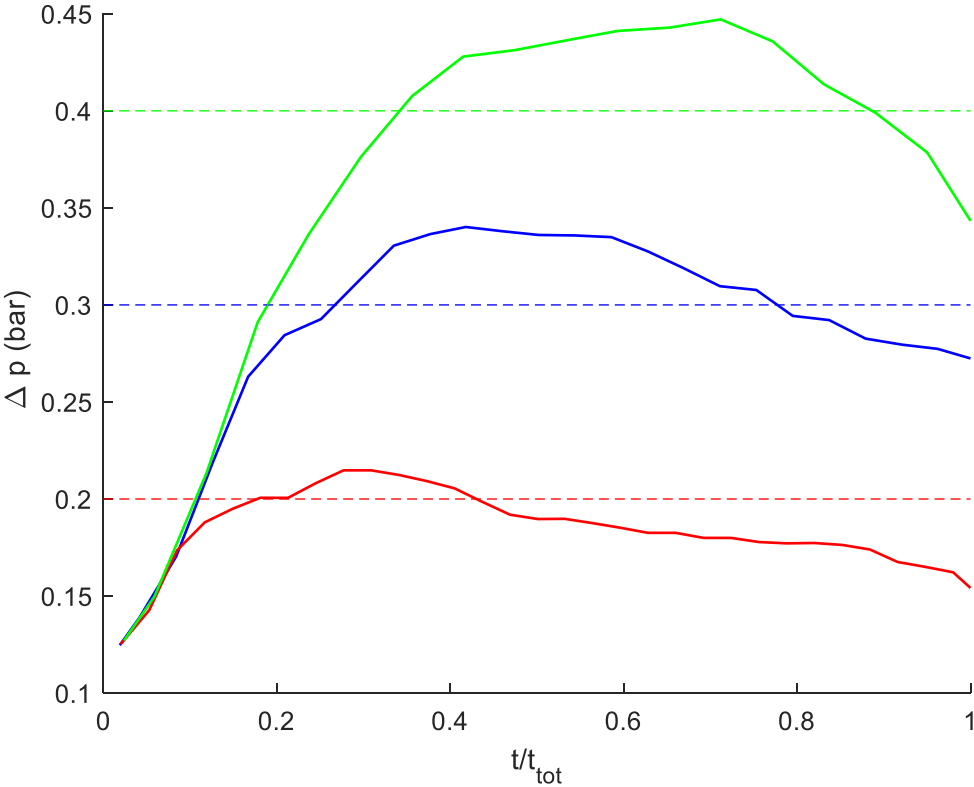


Figure A2. Simulated pressure drops in the pipe system for Experiment 1 (0.3 bar, blue line), Experiment 2 (0.2 bar, red line) and Experiment 3 (0.4 bar, green line).

LIST OF SYMBOLS

Roman

| | |
|-----|------------------------------------|
| A | cross-section area, m^2 |
| d | total distance (cf. Eqs. (1-2)), m |
| f | pressure loss factor, - |
| h | height, m |
| l | length, m |
| p | pressure, Pa |
| r | radius, m |
| Re | Reynolds number |
| t | time, s |
| w | velocity, m s^{-1} |
| V | volume, m^3 |

Greek

| | |
|----------|--|
| α | angle, $^\circ$ |
| μ | dynamic viscosity, Pa s |
| ρ | density, kg m^{-3} |
| ξ | share of wall perimeter touched by core flow |

Subscripts

| | |
|------|----------------------------------|
| 0 | initial state |
| down | lower |
| exp | expansion |
| g | gas |
| i | index for pipe section number |
| in | inlet |
| j | index for element in pipe system |
| l | liquid |
| o | oil |
| out | outlet |
| red | reduction |
| s | core flow |

| | |
|-----|-------|
| tot | total |
| up | upper |
| w | water |

A dot above a symbol denotes a flow rate.

References

- [1] M. Geerdes, H. Toxopeus, C. Van Der Vliet, *Modern Blast Furnace Ironmaking: An Introduction*, 2nd ed.; IOS Press BV: Amsterdam, The Netherlands, **2009**.
- [2] W. B. U. Tanzil, P. Zulli, J. M. Burgess, W. V. Pinczewski, *Trans. Iron Steel Inst. Jpn.* **1984**, *24*, 197.
- [3] W. B. U. Tanzil, *Ph.D. Thesis*, University of New South Wales, Sydney, Australia, **1985**.
- [4] P. Zulli, *Ph.D. Thesis*, University of New South Wales, Sydney, Australia, **1991**.
- [5] L. Shao, H. Saxén, *Ind. Eng. Chem. Res.* **2013**, *52*, 5479.
- [6] T. Fukutake, K. Okabe, *Trans. Iron Steel Inst. Jpn.* **1976**, *16*, 317.
- [7] T. Nouchi, M. Yasui, K. Takeda, *ISIJ Int.* **2003**, *43*, 175.
- [8] Q. He, P. Zulli, G. M. Evans, F. Tanzil, *Dev. Chem. Eng. Mineral Process.* **2006**, *14*, 249.
- [9] Q. He, G. Evans, P. Zulli, F. Tanzil, *ISIJ Int.* **2012**, *52*, 774.
- [10] W. Liu, L. Shao, H. Saxén, *Metals* **2020**, *10*, 496.
- [11] M. Iida, K. Ogura, T. Hakone, *ISIJ Int.* **2008**, *48*, 412.
- [12] M. Iida, K. Ogura, T. Hakone, *ISIJ Int.* **2009**, *49*, 1123.
- [13] J. Brännbacka, J. Torrkulla, H. Saxén, *Ironmak Steelmak.* **2005**, *32*, 479.
- [14] J. Brännbacka, H. Saxén, *Chem Eng Sci.* **2004**, *59*, 3423.
- [15] H. Saxén, *Metall. Mater. Trans. B* **2015**, *46*, 421.
- [16] L. Shao, H. Saxén, *ISIJ Int.* **2011**, *51*, 228.
- [17] M. Roche, M. Helle, J. van der Stel, G. Louwerse, J. Storm, H. Saxén, *Metall. Mater. Trans. B* **2020**, *51*, 1731.
- [18] K. Nishioka, T. Maeda, M. Shimizu, *ISIJ Int.* **2005**, *45*, 669.
- [19] K. Nishioka, T. Maeda, M. Shimizu, *ISIJ Int.* **2005**, *45*, 1496.
- [20] G. M. Park, D. J. Lee, J. H. Lee, H. S. Yoon, *J. Comput. Fluids Eng.* **2016**, *21*, 110.
- [21] M. Vångö, C. Feilmayr, S. Pirker, T. Lichtenegger, *Appl. Math. Model.* **2019**, *73*, 210.
- [22] F. Bambauer, S. Wirtz, V. Scherer, H. Bartusch, *Powder technol.* **2018**, *334*, 53.

- [23] W. Liu, D. N. Mondal, L. Shao, H. Saxén, *Ironmak. Steelmak.* 2020, DOI: 10.1080/03019233.2020.1767395.
- [24] R. J. Nightingale, F. W. B. U. Tanzil, *Iron & Steelmaker.* **1997**, 24, 35.
- [25] N. Brauner, *Modelling and Control of Two phase phenomena: Liquid-Liquid Two Phase Flow Systems*, CISM Center, Udine, Italy, **2002**.
- [26] A. Bensakhria, Y. Peysson, G. Antonini, *Oil & Gas Sci. Tech.* **2004**, 59, 523.
- [27] Neutrium, Engineering knowledge base. <https://neutrium.net/fluid-flow/pressure-loss-from-fittings-expansion-and-reduction-in-pipe-size/>